Institute of Geosciences | Geophysics | Seismology | Volcanology

MuRAT: Multi-Resolution seismic Attenuation Tomography

Luca De Siena

Associate Professor of Geophysics with Volcanology

Head of the Seismology Work-Group

Honorary Lecturer at the University of Aberdeen, UK

work phone: +49 (0)61313928499

cell: +44 (0) 7478686067

email: ldesiena@uni-mainz.de

internet: www.lucadesiena.com

MuRAT in Brief

MuRAT is a Matlab Package for Seismic Attenuation, Scattering and Absorption Tomography using Body and Coda Waves.

Features

What it does: *MuRAT* is a software package for measuring seismic attenuation, scattering, and absorption from passive and active data, and model 3D variations of these parameters in space.

The first MuRAT: *MuRAT1.0* was developed by Luca De Siena during his PhD at the INGV-Osservatorio Vesuviano, Italy, and ***published in 2014*** while he was research assistant at the Westfälisches Wilhelms Universität, Münster. Three sample papers published using this code are: ***De Siena et et al. 2017, SR***, ***Prudencio et al. 2020***, and ***Sketsiou et al. 2021***;

In 2D: ***MuRAT2D*** is the result of the activity of the ***Volcano Earth Imaging group***. It produces 2D seismic scattering and absorption maps at multiple frequencies and is suited for largely undetermined problems. Three sample papers published using this code are: ***De Siena et et al. 2017, GRL***, ***Napolitano et al. 2020***, and ***Sketsiou et al. 2020***;

In 3D: ***MuRAT3D*** is the current standard for measuring total attenuation, scattering and absorption - the project started in 2021 and there are still no published papers. This guide describes this code.

Contents

Chapter 1

Introduction

MuRAT is about imaging the Earth with seismic waves (*seismic tomography*); however, it does not follow the traditional path of imaging *seismic velocity* with travel times, or *phase/group velocities* using surface-waves. MuRAT is a code for *seismic attenuation tomography*. To understand the difference consider the following seismogram, produced by a volcanic earthquake:

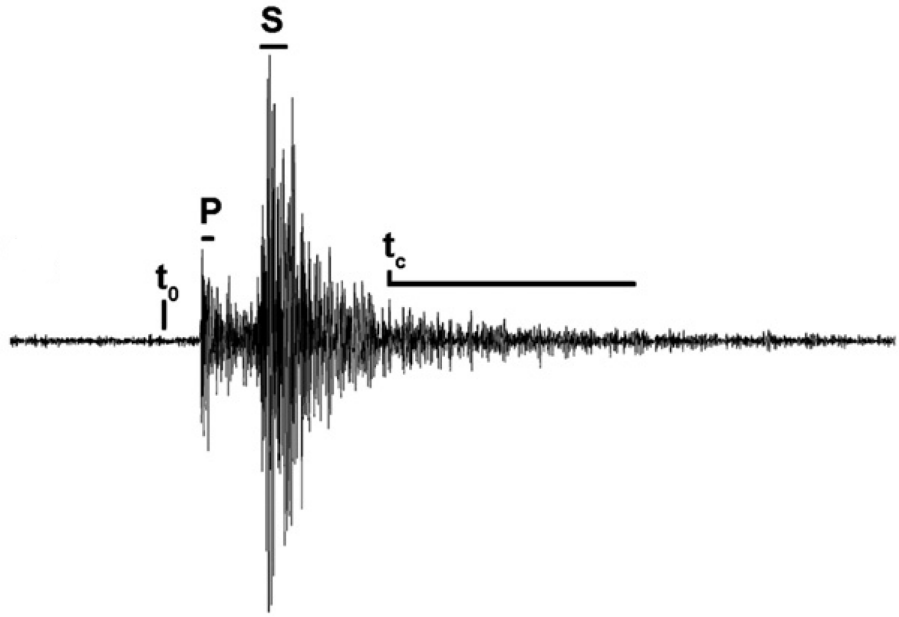

Figure 1.1: A seismogram. MuRAT measures the heterogeneous loss of seismic energy using different seismic attributes

We are used to picking phases on it - for example, the P-wave arrival. By modelling the source-station path followed by the corresponding wave packet with a *ray-tracing* approach, we measure velocity changes over different paths. Travel-time tomography requires a *non-linear inversion*, where we need to update the paths followed by the waves, the corresponding velocity model, and seismic locations jointly to find a reliable solution. There are multiple codes that do this: our favourites are LOTOS

and FMTOMO - just click on their names to go to their internet site. However, MuRAT is part of a wider framework working across multiple langiages (Matlab, Python and Julia). This comprises codes that allow the user to measure and image body-wave and surface wave velocity in space (from earthquake and noise) (seispy, interfaced with python) and full waveform inversions (FWI, in Julia). This framework especially couples seismology with outputs from Geodynamics codes efficiently. It is highly recommended to combine MuRAT with the partner codes for a complete imaging of the area under study.

MuRAT deals with the loss of energy suffered by seismic waves while they propagate through the heterogeneous Earth. It fills the gap of an open-access tool to measure attenuation, separate the processes that lead to it, and model them in space. To our knowledge, the first mention of an *attenuation tomography* was given by Ho-Liu et al. (1988) in the Coso Valley. More than 30 years afterwards, this technique is a standard with applications at the global, regional and local scales. Yet, different mechanisms attenuate seismic waves while they propagate. While codes to model total attenuation in space exist, no open-access code can measure attenuation, separate the mechanisms that produce it and model their variations in space with seismic inversion. No code can certainly do it using as input seismograms downloaded from the data servers.

We define here the mechanisms causing seismic attenuation:

1. Seismic energy progressively spreads over larger volumes while propagating far from the source. Energy thus decreases with distance due to *geometric spreading*. This mechanism is independent of frequency for a given phase. However, depending on frequency, often more than one phase are included in a *window of time* measured on a seismogram - in Fig. 1.1 it is challenging to distinguish between S-waves and surface waves produced right after them.

2. Seismic energy is lost into the heterogeneous Earth depending on the ratio between the wavelength (λ) and the dimension of the heterogeneity (a). Energy thus decreases with distance due to *scattering losses*. This mechanism depends on frequency and comprises complex physics, as those described by multi-pathing and diffractions. Reflection and refraction can be described as scattering processes.

3. Seismic energy interacts with the heterogeneous Earth losing heath for each cycle. Energy thus decreases with distance due to *absorption losses* in the materials they pass through. This mechanism depends on frequency. How much energy the Earth actually absorbs is difficult to quantify, but such a quantification allows connecting seismology with other disciplines.

4. The sum of scattering and absorption losses gives *total attenuation*. This is the attenuation experienced by direct wave-packets while they propagate through the heterogeneous Earth. When we talk about seismic attenuation we generally refer to total attenuation. However, this is only valid in specific circumstances and for specific phases.

MuRAT measures and models total attenuation, scattering attenuation and absorption in space using single seismogram observations. The first three chapters offer an overview of the theory underlying attenuation tomography in these three forms.

In chapter 2, we revise the theory behind measurement and modelling of the energy lost by direct waves (**P** and **S**, Fig. 1.1). MuRAT uses the standard description of geometric spreading, r^{α}, with r is the hypocentral distance and α the geometric spreading coefficient. This description is contested by some authors (Morozov, 2008), who use a simpler, line-fitting approach and remove difference between scattering and absorption losses. This approach has been fiercely contested by other authors (Xie, 2010). **MuRAT measures α with its uncertainty.** By comparing the results to the assumed value of α for direct wave energiess ($\alpha = 1$) the user knows how far this is from the theory. At present, this is all that MuRAT will do to tackle geometric spreading; however, a lot of what is done by the code depends on this debate, among others the applicability of Multiple-Lapse-Time-Window-Analysis (MLTWA - Fehler et al. (1988)).

The method used to model total attenuation in chapter 2 is the *coda normalisation* (CN) (Aki, 1980; Yoshimoto et al., 1993). In tomography, the method has been introduced by Del Pezzo et al. (2006). At the core of MuRAT, there is this seminal paper, which has been developed by De Siena et al. (2009) and De Siena et al. (2010) for muti-scale applications. De Siena et al. (2010) benchmark the CN with the standard spectral slope (t^*) method, applied by the global community. For a decade, the method has only been applied to volcanoes. The reason is the need for a relevant *coda* (t_c, Fig. 1.1) to normalise direct-wave information. The method has the great advantage of removing source and site effects from direct wave measurements, but suffers from an inexact description of the process. **MuRAT3D deals with this problem, using theoretical and computational results obtained in the last decade.**

In chapter 3, we revise the theory behind the use of *peak delays* as markers of scattering losses (Saito et al., 2002; Takahashi et al., 2007, 2009; Tripathi et al., 2010; Calvet and Margerin, 2013; Calvet et al., 2013; De Siena et al., 2016; Sato, 2016). Peak-delays are the focus of the early-warning community

and a quantity important to seismic source modelling in the near field. The standard theory recognises peak delay as a marker of scattering losses in the far field, modelled by the Markov approximation (Saito et al., 2002), in the case scattering is produced only by long wavelength component ($\lambda << a$. However, recent research suggests a dependence of peak-delay on scattering when λ is of the order of propagation distance and correlation length of heterogeneity (Napolitano et al., 2020; Di Martino et al., 2021). Here phenomena like diffraction and trapping take over. **The chapter discusses the standard application, theoretical limitations and future outlooks.**

In chapter 4, we revise the theory behind the use of *late-time coda attenuation* as marker of seismic absorption (Wegler and Lühr, 2001; Prudencio et al., 2013; Calvet and Margerin, 2013; Del Pezzo et al., 2016; De Siena et al., 2016, 2017a; Del Pezzo et al., 2018; Sketsiou et al., 2020). Coda attenuation can be described using single and multiple scattering. MuRAT provides the tools to test the onset of equipartition, a necessary condition for diffusion, where coda attenuation is equivalent to seismic absorption. The embedded sensitivity kernels model coda attenuation in space based on Paasschens equations (Paasschens, 1997) and the approximations of Pacheco and Snieder (2005). The theory is inexact in the case of sharp vertical or lateral boundaries. The work of Morozov (2008) implies that diffusion never onsets. However, in zones where the Moho is thick ad for sufficient amount of data, the theory generally produces stable results (Sketsiou et al., 2020). New work has been recently developed to include the effect of sharp boundaries and vertical velocity variations on coda attenuation measurements (Sanborn et al., 2017; Cormier and Sanborn, 2019). **MuRAT currently provides the tool to invert for coda attenuation using a diffusive approximation and sensitivity kernels**.

From chapter 5, this manual describes how to use the code, so you can skip there if you already know the theory.

Chapter 5 describes installation procedures for MuRAT. MuRAT 3.0 comes into Matlab and Julia packages. We discuss why the code is released in proprietary and non-proprietary languages. Installation procedures are straightforward in both cases.

Chapter 6 describes data specifications for MuRAT. MuRAT 3.0 accepts only Seismic Analysis Code (SAC) data. SAC is a standard for seismologists, and the favourite format when converting miniseeds on data servers like IRIS. It is possible you have been processing data with another software. In this chapter, we will discuss the conversions necessary to create a readable dataset for MuRAT.

Chapter 7 describes input files for MuRAT. We offer three example applications (Campi Flegrei caldera, Italy - Mount St. Helens, US - Vrancea, Romania) each with its input files. In theory, these are the

only files the users need to edit, once data files are in the correct format.

Chapter 8 describes the data processing functions. These functions are editable by the user or can be completely overridden in case data processing is performed with another software. We describe the input necessary to these functions and the output produced.

Chapter 9 describes the forward modelling. MuRAT performs both ray tracing and sensitivity kernel modelling for coda waves. As before, if you have a favourite ray tracing or coda-sensitivity modelling algorithm you can skip this part. We describe the input necessary to these functions and the output produced. At present MuRAT models peak-delay and CN measurements using rays and coda attenuation via sensitivity kernels.

Chapter 10 describes the regionalisation and inversion procedures. Peak delays are regionalised, the other two attributes are inverted.

Chapter 11 describes file outputs and plotting. MuRAT provides outputs in Matlab and Paraview formats. Figures are saved in Matlab for post-processing.

Chapter 2

Direct-wave attenuation: Q

Timeline in papers.		
Paper	**Descriptor**	**Where**
(Aki and Chouet, 1975)	S-wave CN method	Link
(Yoshimoto et al., 1993)	P-wave CN method	Link
(Del Pezzo et al., 2006)	S-wave CN tomography	Link
(De Siena et al., 2010)	Benchmark with t^* method	Link
(De Siena et al., 2014a)	MuRAT1.0 for CN method published	Link
(De Siena et al., 2014b)	P-wave coda-normalisation tomography	Link
(Prudencio et al., 2015)	Active CN tomography	Link
(De Siena et al., 2017a)	CN tomography measuring Qc	Link

2.1 Parameters

Input Parameters for MuRAT		
Symbol	**Descriptor**	**Where**
t_P or t_S (s)	P-wave or S-wave arrivals	SAC Haeder
t_l (s)	Length of P- or S-wave window	Set in input file
t_0 (s)	Origin time	SAC Haeder
t_c (s)	Lapse time from origin time	Set in input file
t_w (s)	Length of coda window	Set in input file

2.2 The coda normalisation method in pills

The method measure direct and coda-wave energies and divides them to obtain a quantity that only depends on Q, allowing for a linearized inversion.

Pros of measuring direct-wave attenuation using coda-normalised energies

1. Single-station measurements - you can get all the info from a single seismogram.
2. No need for correcting source and site effects - these are particularly relevant in the heterogeneous Earth.

Cons of measuring direct-wave attenuation using coda-normalised energiess

1. Uncertain sensitivity of coda waves to Earth structures - the assumption of homogeneous coda wave sensitivity is generally unfulfilled. *Tackled by MuRAT estimating the measurable coda-wave energy at the chosen lapse time and assuming a diffusive behaviour.*

2. Correction of radiation pattern - increasing direct wave windows smooths it at the expense of focusing. *Tackled by working with different windows to measure direct-wave energy.*

Figure 2.1 is a visual representation of the method.

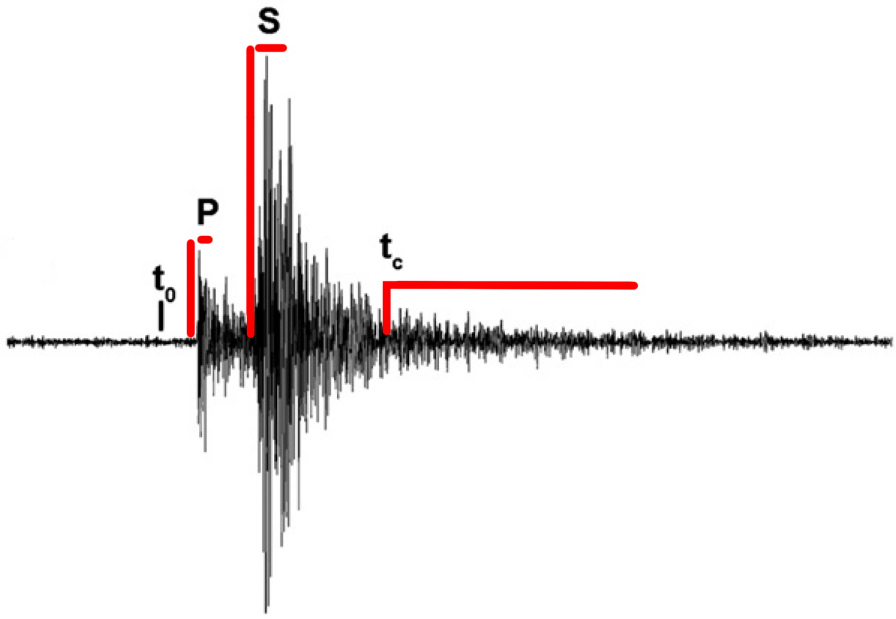

Figure 2.1: The CN method measures the spectral energies of direct and coda waves and inverts for Q. In red the P and S wave energies and the normalizing coda energies.

2.3 The theory bit

The coda-normalisation (CN) method normalises P- and S-wave energy for coda energy (Aki, 1980; Yoshimoto et al., 1993). Seismic wave energies can be modelled as the convolution of the source, path, site, and instrument functions, so that the spectral energy of direct waves (E) is:

$$E(f,r) = R_{\theta\phi} S_S(f) r^{-\gamma} I(f) G(f,\Psi) \exp\left(-\frac{2\pi f}{Q(f)v} r\right) \tag{2.1}$$

where $\boldsymbol{f}$ is the frequency, r is the source-receiver distance, t_c is the coda-wave central lapse time from the origin time of the event (t_0), $R_{\theta\phi}$ is the source radiation pattern (θ and ϕ the azimuth and take-off angle for a source-receiver ray), $S_S(f)$ is the source function, γ the geometrical spreading exponent, $I(f)$ the known instrumental response, $G(f,\Psi)$ is the site amplification factor (with Ψ being the incident angle of the ray at the station), Q is the direct-wave quality factor and v the average velocity in the medium (Yoshimoto et al., 1993).

The spectral energy of coda waves (E_c) can be written as:

$$E_c(f,t_c) = S_S(f)P(f,t_c)G(f)I(f). \tag{2.2}$$

The attenuation of coda waves can then be expressed as (Aki and Chouet, 1975):

$$P(f,t_c) \simeq t_c^{-n} \exp\left(-2\pi f Q_c^{-1} t_c\right) \tag{2.3}$$

In this equation, n is the envelope spectral decay, Q_c is the coda quality factor, and $A_c(f,t_c)$ does not include the effect of the source radiation pattern. We will discuss moire about this term in chapter 4.

Eq. 2.1 can be divided by Eq. 2.2 to normalize the energy of the spectral energy of direct waves using the spectral energy of coda waves:

$$\frac{E(f,t_c)}{R_{\theta\phi}E_c(f,t_c)} = r^{-\gamma}\frac{G(f,\Psi)}{G(f)}\exp\left(-\frac{2\pi f}{Q(f)v}r\right)\frac{1}{P(f,t_c)} \tag{2.4}$$

where the source function $S_S(f)$ and the instrumental response $I(f)$ contributions disappear. By measuring direct-wave energy over a window of sufficient length (t_l), we smooth the azimuthal contribution of the radiation pattern (De Siena et al., 2009, 2010). If the length of the direct-wave window is chosen appropriately, the contribution of the source radiation pattern $R_{\theta\phi}$ is negligible (De Siena et al., 2009) so that $R_{\theta\phi} = 1$ and $\frac{G(f,\Psi)}{G(f)} = 1$. Since early coda consists of randomly scattered waves, the coherency and the source radiation pattern is eventually lost (Takemura et al., 2009). De Siena et al. (2010) demonstrate that a coda window of 2 s is sufficient to make the radiation pattern quasi-isotropic in a volcanic caldera. Still, the window length must be carefully chosen at each frequency to avoid near-receiver onset of surface waves (Gabrielli et al., 2020).

At fixed frequency band and starting lapse-time for coda windows, $P(f,t_c)$ is assumed to be constant in the standard coda-normalisation method (Del Pezzo et al., 2006; Sato et al., 2012). Taking the

logarithm, Eq. 2.4 becomes:

$$\ln\left[\frac{E(f,t_c)}{E_c(f,t_c)}\right] = -\ln P(f,t_c) - \gamma \ln(r) - \frac{2\pi f}{Q(f)v} r, \tag{2.5}$$

a linear equation solved for three unknown ($\ln P(f,t_c)$, γ, Q) once the hypocentral distance is known and the frequency is set. If Q_c is known for each source station pair, one can pre-estimate $P(f,t_c)$ using equation 2.3, as done by De Siena et al. (2017b):

$$\frac{1}{2\pi f}\ln[\frac{E(f,t_c))}{E_c(f,t_c)} + \frac{1}{2\pi f}\ln P(f,t_c) = -\frac{\gamma \ln(r)}{2\pi f} - Q(f)^{-1}t, \tag{2.6}$$

where t is the travel time of the corresponding direct phase. The system can be solved with a linear inversion for γ and $Q(f)^{-1}$. This is the method implemented in MuRAT3.0.

2.3.1 Applicability

For the applicability of the CN method, one must measure direct-wave energy. This seems simple enough, but it can become very problematic depending on frequency, heterogeneity and source-station distance. To check the validity, one must always look at relationship between direct-wave energy and epicentral distance. Is there a dependence? If not, near field or strong scattering might be prevalent. Does the relationship follow standard geometrical spreading, like those for direct wave energy? How important is the surface wave component? A positive is that generally where you cannot measure *direct-wave energy*, you can use codas, i.e., diffusion onsets pretty quickly (see chapter ??).

2.4 MuRAT workflow

MuRAT works in analogy to De Siena et al. (2010), De Siena et al. (2014a) and Sketsiou et al. (2021) when mapping peak delays. These authors show that one must check the relationship between hypocentral distance (or travel time) and measured energy ratio. In Figures 2.2, we show an example at Mount St. Helens volcanoes, where sources and stations can be either on or inside the volcanic edifice and near surroundings (red dots) or far from them (cyan dots). The expected decrease of energy with hypocentral distance is unfulfilled at small distances, where surface and trapped waves dramatically increase coda energy. The energy in the coda can be back-traced to mark the position and intensity of the corresponding scatterers (De Siena et al., 2014b), using scattering tomography (also known as

Nishigami (1991) technique). The method can still be applied, but fixing the geometrical spreading will trade-off measurements at low frequencies. Sketsiou et al. (2020) discusses the corresponding trade-offs in volcanic, fault and regional settings. In Fig. 2.3 we show the same plot for the normalised S-wave energy at Mount Vesuvius, where all sources and stations are inside the more heterogeneous domain of the volcanic edifice and feeding system. Here, only data at 18 Hz can be used.

Following De Siena et al. (2014a), measurements above (below) the logarithmic linear trend shows high (low) attenuation. This procedure is inverted by this version of MuRAT using a ray bending approach (Block, 1991; De Siena et al., 2010), discussed computationally in Chapter ???.

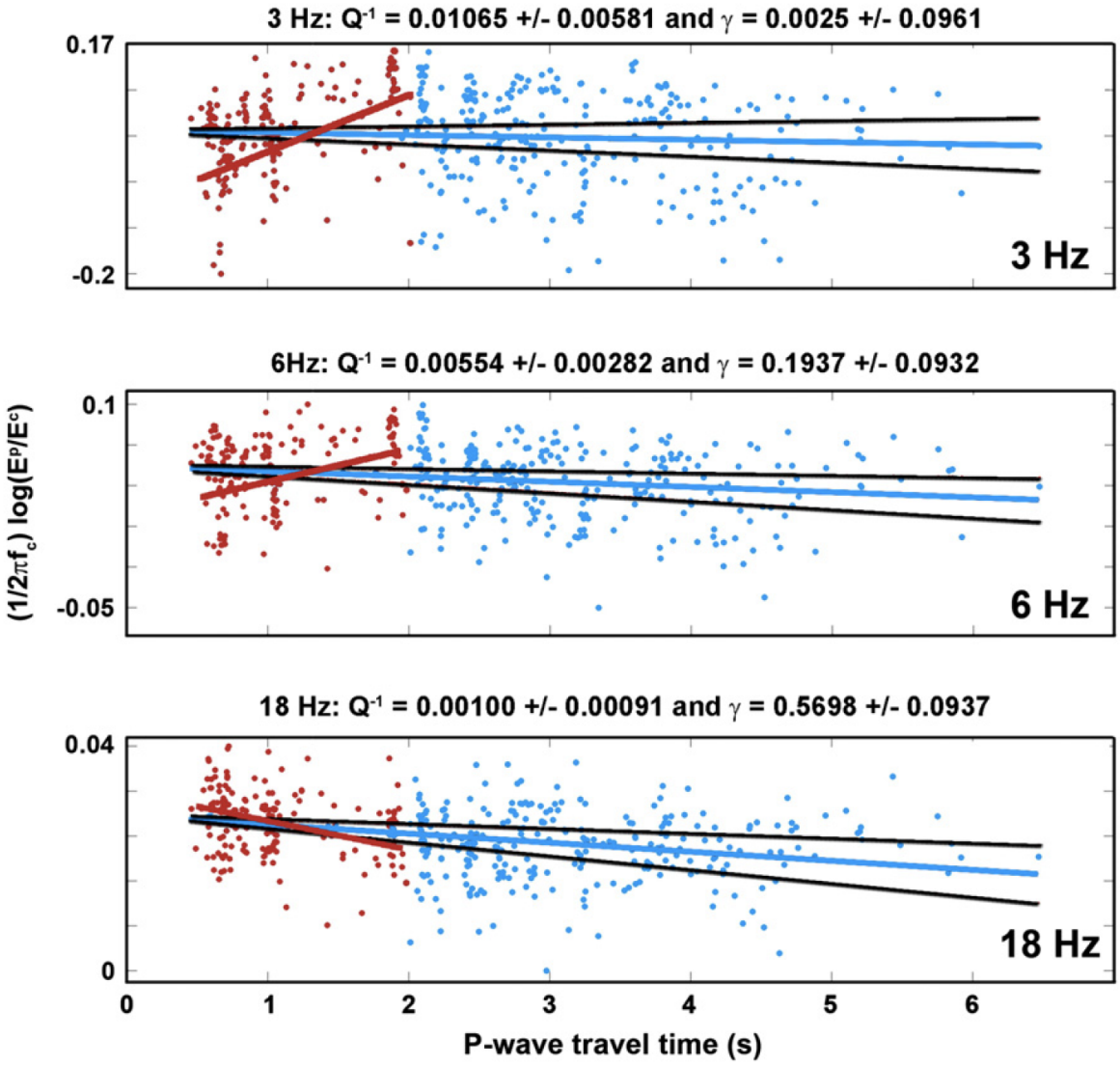

Figure 2.2: A plot of the logarithm of the P-wave direct-to-coda energy ratios (red and cyan dots, computed at MSH in three frequency bands) versus the P-wave travel times at Mount St. Helens volcano. The red lines show the linear fit that would be obtained by using only data between travel times of 0 and 2 s, affected by surface waves inside the volcanic edifice. The cyan lines represent the least squares fit the entire dataset. The black lines correspond to maximum uncertainties. The geometrical spreading and the average Q obtained from the inversion for the average parameters are shown above each plot. Notice the progressive change with increasing frequency. From De Siena et al. (2014a).

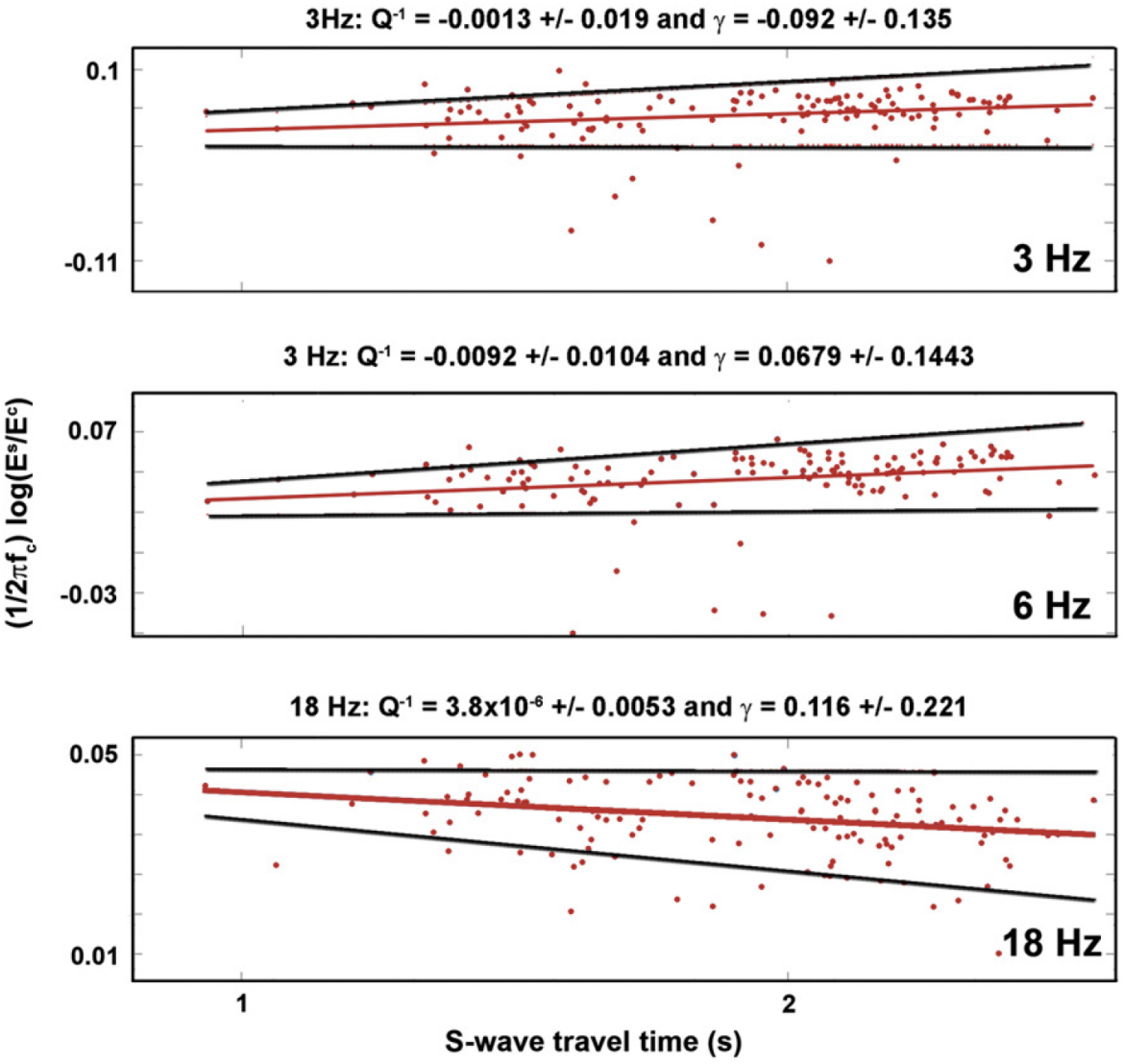

Figure 2.3: Same as Fig. 2.2 for Mount Vesuvius, where earthquakes and stations are all comprised under the volcanic edifice. Notice the negative Q at low frequencies. From De Siena et al. (2014a).

Chapter 3

Scattering attenuation: *peak delays*

Timeline in papers.		
Paper	**Descriptor**	**Where**
(Saito et al., 2002)	Markov approximation	Link
(Takahashi et al., 2007)	Peak-delay regionalisation	Link
(Takahashi et al., 2009)	Peak-delay tomography	Link
(Calvet et al., 2013)	Peak delay regionalisation + Qc: crust	Link
(De Siena et al., 2016)	Peak delay + Qc: volcano	Link
(Sato, 2016)	Peak delays - short and long λ	Link

3.1 Parameters

Input Parameters for MuRAT		
Symbol	**Descriptor**	**Where**
t_{min}	minimum peak delay allowed	Set in input file
t_{max}	maximum peak delay allowed	Set in input file
t_0 (s)	Origin time	SAC Haeder

3.2 The peak delay method in pills

The method measures the delay of the maximum energy of the envelope of the direct way to model scattering attenuation with regionalization.

Pros of measuring scattering attenuation using peak delay

1. Single-station measurements - you can get all the info from a single seismogram.
2. Proven sensitivity to structural information and geologic boundaries.

Cons of measuring scattering attenuation using peak delay

1. Assumptions underlying the Markov approximation could be unfulfilled. *Tackled by MuRAT estimating parameters at different frequecies.*
2. No inversion, only regionalization. *Still not tackled by MuRAT.*

Figure 3.1 is a visual representation of the method.

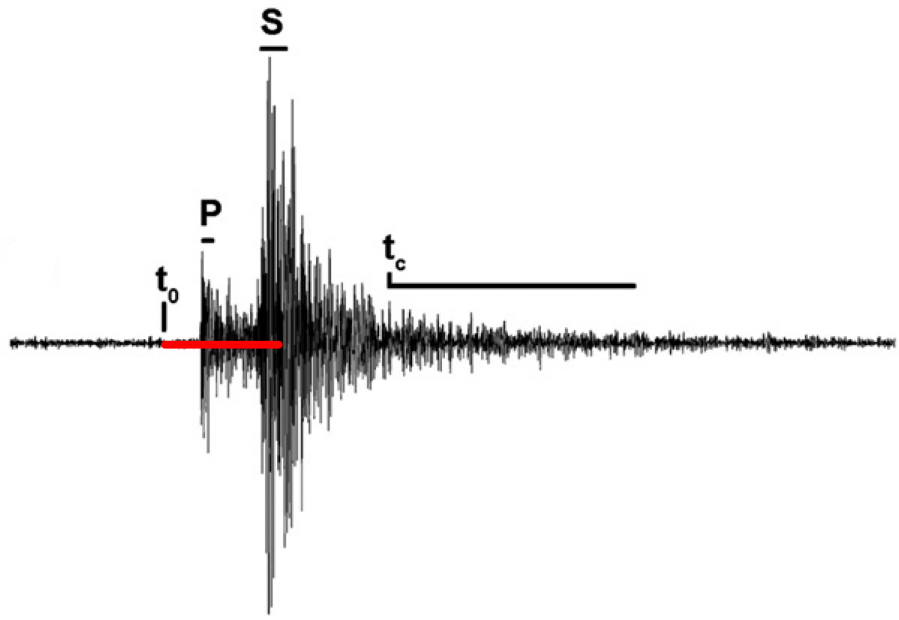

Figure 3.1: The PD method measures the delay of the maximum of the envelope from either the arrival time or the origin time of the event.

3.3 The theory bit

While travelling, direct wave packets broaden because of scattering and diffraction. The seminal work for the application of *peak delay* (envelope broadening) imaging are Aki and Chouet (1975), who demonstrate that coda of high-frequency seismograms originate from random inhomogeneity in elastic properties, and (Sato, 1989), who first proposed peak-delays as a tool to characterise random heterogeneity. Fehler et al. (2000) proved that the Markov approximation for the parabolic wave equation can synthesise seismic waveforms in two dimensions, including early and intermediate coda. The seminal work for the technique is Saito et al. (2002), who developed the equations for forward modelling envelopes for spherically outgoing media characterised by von Kármán power spectral density functions (PSDF).

Saito et al. (2002) provides both an historical view and a discussion of the assumptions underlying the method:

- The primary assumption of the method is that the wavelength ($\lambda = 2\pi/k$) is smaller than the

correlation distance (a), so that if this is multiplied by the wavenumber: $ak >> 1$. Obviously, the estimation of a is challenging but it appears likely that the assumption will be broken at low frequencies, where *diffraction* takes over.

- Propagation is entirely constrained within a single parallelepiped of average velocity V_0. The velocity field depends on space (r) as:

$$V(r) = V0(1 + \xi(r)) \tag{3.1}$$

where $\xi(r) << 1$ are random velocity fluctuations. For a wider description of how to derive auto-correlation and power spectral density functions describing fluctuation distributions refer to Sato et al. (2012). These quantities are controlled by ϵ (the root-mean-square of velocity fluctuations), a (the correlation length) and κ (tuning the richness of short-wavelength components of the random medium).

- Frequencies are above 1 Hz, as below that the wavelength grows to a level where most assumptions are invalid in lithospheric settings.

The original definition models envelope duration (t_q) as the quantity related to the characteristic time of envelope broadening (t_M) (Saito et al., 2002). It is instructive to look at the definition of t_M given by Sato (2016):

$$t_M(\kappa, \zeta, k_c, r_0) = \frac{\epsilon^2}{2V_0 a} C_L(\kappa, \zeta, k_c) r_0^2; \tag{3.2}$$

where ζ, which is a number varying between 0.25 and 1.75. Sato (2016) defines it as a tuning parameter and separates random media between long- and short-scale components, so that the correlation distance for small-scale component is : $a_S^{-1} = \zeta k_c$.

This quantity fully defines scattering in the case of long wavelength heterogeneities, depending on average velocity (V_0), hypocentral distance (r_0, which in a homogeneous medium is the product of V_0 and travel time of the phase t), correlation distance (a), and mean squared velocity fluctuations (ϵ^2), the wavenumber, depending on the angular frequency (ω_c) as $kc = \frac{\omega_c}{V_0}$ and where:

$$C_L(\kappa, \zeta, k_c) = \begin{cases} \frac{\pi^{1/2}\Gamma(\kappa+\frac{1}{2})}{(2\kappa-1)\Gamma(\kappa)}(1 - (\zeta a k_c)^{1-2\kappa}) & \kappa \neq \frac{1}{2} \\ 2ln(\zeta a k_c) & \kappa = \frac{1}{2} \end{cases} \tag{3.3}$$

The dependency on V_0 and a seem straightforward, at least until we do not make r_0 and $C_L(\kappa, \zeta, k_c)$ explicit. Let's see what happens for $\kappa = \frac{1}{2}$:

$$t_M(\kappa = \frac{1}{2}, \zeta, k_c, r_0) = \frac{\epsilon^2}{2V_0 a} V_0^2 t^2 2ln(\zeta a k_c) = \frac{\epsilon^2 V_0 t^2 ln(\zeta a k_c)}{a}; \tag{3.4}$$

in which case:

- The characteristic time increases quadratically with travel time, hence the need for correcting this dependency to focus on scattering.
- A sure way to increase scattering is to increase ϵ^2 -beware that these variations are generally limited.
- Characteristic times increase with frequency and ζ although only logarithmically.
- For actual ranges of correlation distances, t_M can change a lot.

3.3.1 Applicability

The important assumption for the applicability of peak-delay analysis is that scattering is produced by long-scale components. To check the validity, one must always test the following conditions: $\zeta a k_c >> 1$. In general, this means frequency above 1 Hz. In this case, we can rewrite:

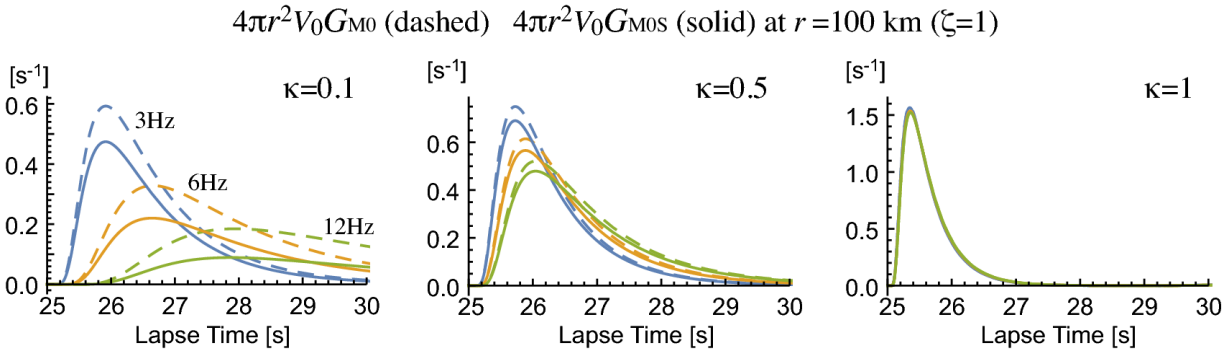

Figure 3.2: Broadening for different κ values. For parameters used, see Sato (2016).

$$t_M(\kappa,\zeta,k_c,r) = \begin{cases} \frac{\epsilon^2}{2V_0 a} r^2 \frac{\pi^{\frac{1}{2}}\Gamma(\kappa+\frac{1}{2})}{(1-2\kappa)\Gamma(\kappa)} (\zeta a k_c)^{1-2\kappa} & \kappa < \frac{1}{2} \\ \frac{\epsilon^2}{2V_0 a} r^2 ln(\zeta a k_c) & \kappa = \frac{1}{2} \\ \frac{\epsilon^2}{2V_0 a} r^2 \frac{\pi^{\frac{1}{2}}\Gamma(\kappa+\frac{1}{2})}{(2\kappa-1)\Gamma(\kappa)} & \kappa > \frac{1}{2} \end{cases} \tag{3.5}$$

This is probably the most important relationship as it shows the lack of changes with frequency for $\kappa > \frac{1}{2}$ and the slow dependency for $\kappa = \frac{1}{2}$. Characteristic times, envelopes and scattering are strongly frequency-dependent when $\kappa < \frac{1}{2}$. This gives us an immediate test on our data. Do waveform broaden dramatically at high frequencies (Fig. 3.2)? This is already an indication of the richness in long wave numbers (short-scale components). The first check the user should do is then visual on the data.

3.4 MuRAT workflow

MuRAT works in analogy to Takahashi et al. (2007), Tripathi et al. (2010) and Calvet et al. (2013) when mapping peak delays. These authors show that above 1 Hz one must check the relationship between hypocentral distance and measured peak delay. In Figures 3.3-3.4, we show two examples for different hypocentral distances. It is clear that there is a threshold over which you can apply the approximation. Hence Murat shows you the same plot for your dataset - we will discuss in Chapter ?? the examples at Mount St. Helens and in Vrancea. The peak-delay method requires the same ray tracing approach used for the CN method, discussed computationally in Chapter ???.

Following Takahashi et al. (2007), measurements above (below) the logarithmic linear trend shows high (low) scattering. This procedure is regionalized by this version of MuRAT. It means that positive and negative variations are allocated via their average over blocks after raytracing. The variation is weighted by the length of each segment. Takahashi et al. (2009) show that there are better procedure to invert for the characteristics of power spectral density function using peak delay: we leave it for future versions of the code.

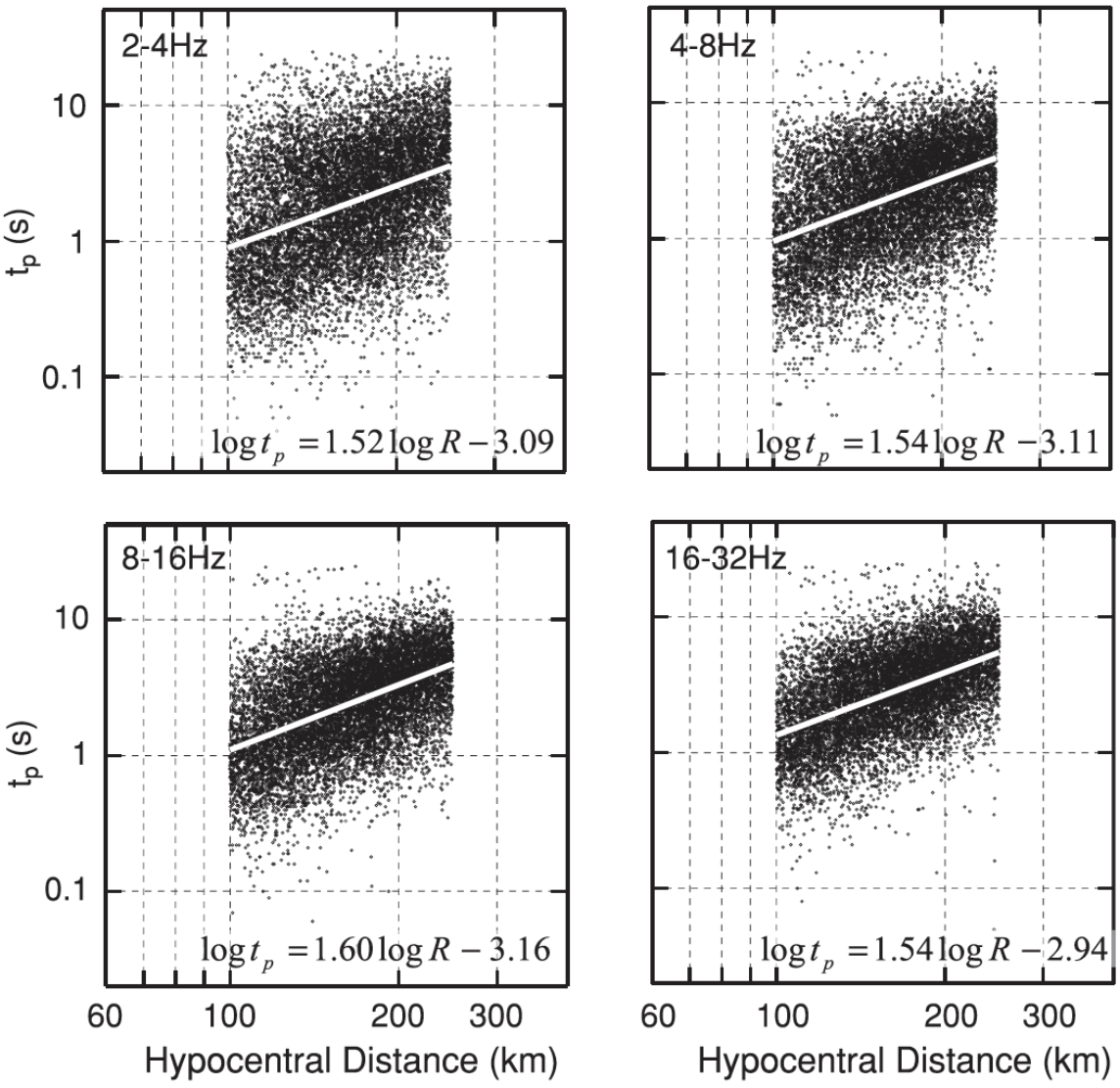

Figure 3.3: Logarithmic plot of peak delay times against hypocentral distances. Black dots represent the data used in this study. White lines are regression lines. From Takahashi et al. (2007).

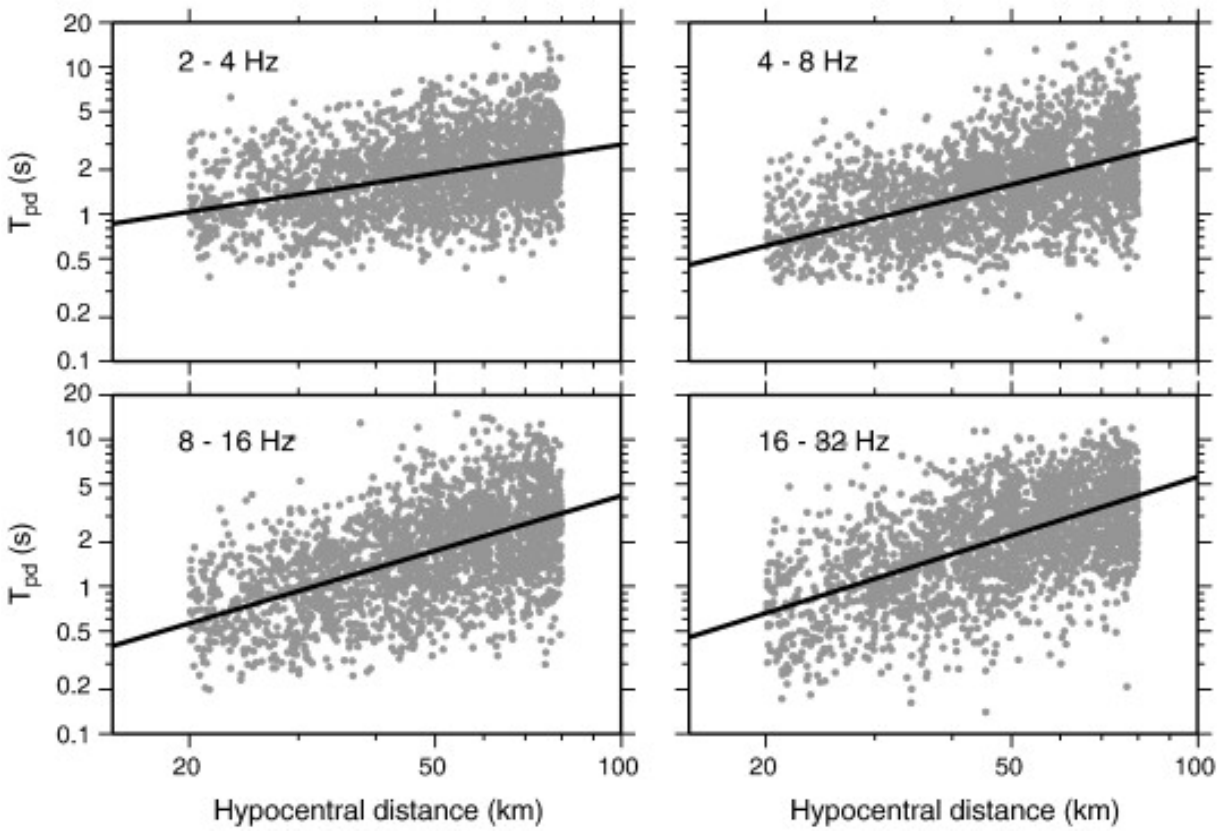

Figure 3.4: Logarithmic plot of peak delay times (in seconds) as a function of the hypocentral distance (in kilometers) for crustal S waves in four frequency bands. Gray dots are the data, and black lines are the regression lines: log10(Tpd) = Ar(f) + Br(f)log10R. From Calvet et al. (2013).

Chapter 4

Absorption: *late time coda attenuation*

Timeline in papers.		
Paper	**Descriptor**	**Where**
(Aki and Chouet, 1975)	Origin of Coda	Link
(Fehler et al., 1992)	MLTWA	Link
(Prudencio et al., 2013)	Qc imaging with Gaussian kernels	Link
(Calvet et al., 2013)	Peak delay regionalisation + Qc: crust	Link
(De Siena et al., 2016)	Peak delay + Qc: volcano	Link
(Del Pezzo et al., 2016)	2D RTT sensitivity kernels: analytic	Link
(De Siena et al., 2017a)	2D inversion with analytic kernels	Link
(Del Pezzo et al., 2018)	3D RTT sensitivity kernels: diffusive	Link
(Akande et al., 2019)	3D inversion with diffusive kernels	Link
(Gabrielli et al., 2020)	MLTWA+2D inversion	Link
(Sketsiou et al., 2020)	Absorption tomography	Link

4.1 Parameters

Input Parameters for MuRAT		
Symbol	**Descriptor**	**Where**
t_k	starting lapse time	Set in input file
t_w	coda window length	Set in input file
t_0 (s)	Origin time	SAC Haeder

4.2 The Qc method in pills

The method measures the decay of the envelope from a given lapse time as a way to model absorption with an inversion procedure.

Pros of measuring absorption using Qc

1. Single-station measurements - you can get all the info from a single seismogram.
2. Proven sensitivity to fluids.
3. High-resolution information on near-source and near-station structures.
4. Full inversion procedure.

Cons of measuring scattering attenuation using peak delay

1. The diffusive assumption is rarely fulfilled, with the onset of surface waves corrupting especially low frequencies. *Tackled by MuRAT estimating parameters at different frequecies.*

2. Assumption of single highly-diffusive layer rarely fulfilled. *Still not tackled by MuRAT.*

Figure 4.1 is a visual representation of the method.

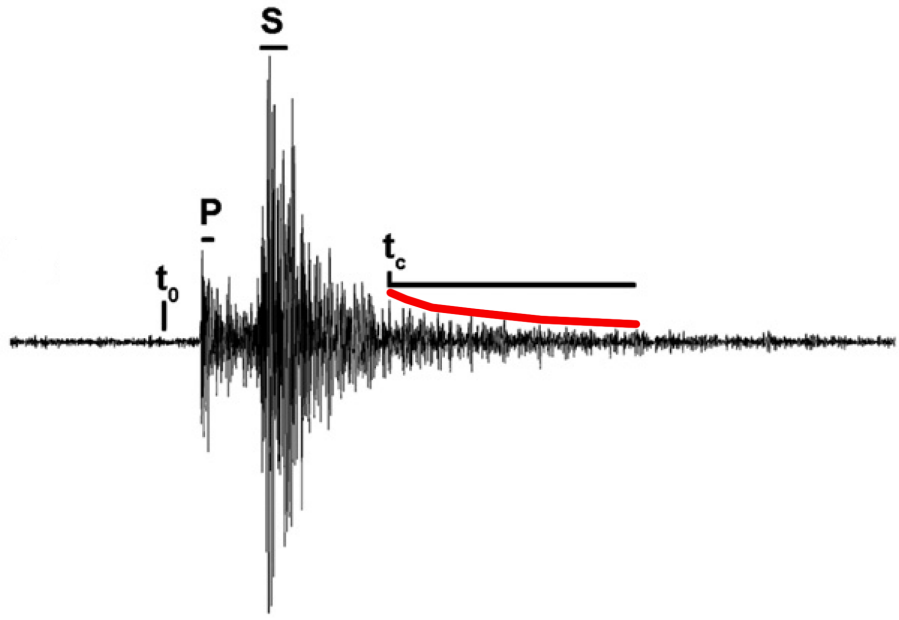

Figure 4.1: The Qc method measures the decay of the envelope from a given lapse time from the origin time of the event.

4.3 The theory bit

4.3.1 MLTWA

Coda waves can be used for more than just normalizing direct wave energies. Starting from the seminal work of Aki and Chouet (1975), coda waves have been used to characterize the tectonic state of the Earth. This has lead to the development of the Multiple Lapse Time Window Analysis (MLTWA) technique Fehler et al. (1992) to separate scattering attenuation Q_s^{-1} from absorption Q_i^{-1}. It does so by measuring extinction length ($L_e = Q_s^{-1} + Q_i^{-1}$) and seismic albedo ($B_0 = \frac{Q_s^{-1}}{L_e}$).

Two assumptions are necessary to apply the MLTWA technique: the direct S-wave dominates the early portion of an S-wave seismogram; the S-coda comprises scattered S-waves. While in its first portion

the S-wave amplitude is controlled by the total attenuation of the medium, coda-waves are a product of scattering (Sato et al., 2012). The filtered seismograms are divided into three time-windows, starting from the S arrival, defined by a starting time t_k and window length t_w. The time integrals $E_k(r)$ of the seismic energy density $E(r,t)$ in each window k is:

$$E_k(r) = \int_{t_k}^{t_k+\Delta t} E(r,t)dt \quad k = 1...3 \tag{4.1}$$

where the energy is still a function of the source-station distance *r*. The wave energy decay for each cycle $-\Delta E/E$ is a function of the total quality factor Q (related to the attenuation coefficient η) via the following equation:

$$-\frac{\Delta E}{E} = \frac{2\pi}{Q} = 2\pi\left(\frac{1}{Q_i} + \frac{1}{Q_s}\right) = \frac{\upsilon\eta}{f} \tag{4.2}$$

where υ is the average wave speed and f is the frequency, respectively. The next step consists in the correction of the energy of each window $E_k(r)$ for both the geometrical spreading and the integral of the t_w-seconds-long normalisation window (the last window in time). This procedure removes source and site effects (Mayeda et al., 1992):

$$E_k^{obs}(r) = \log_{10}\left(4\pi r^2 \frac{E_k(r)}{\int_{t_{coda}}^{t_{coda}+\Delta t} E_k(r,t)dt}\right) \tag{4.3}$$

The resulting logarithms are plotted versus distance in the four frequency bands considered and fitted to the theoretical normalised energies (Fig. **??**). The theoretical curves are modelled using the L2-norm misfit function for a number of waveforms from i to N:

$$M(L_e^{-1}, B_0) = \sum_{i=1}^{N}\sum_{k=1}^{3}[E_k^{obs}(r_i) - E_k^{theo}(r_i, L_e^{-1}, B_0)]^2 \tag{4.4}$$

$E_k^{theo}(r_i, L_e^{-1}, B_0)$ is the theoretical normalised energy computed at distance r_i for the k-th time-window, fixing the L_e^{-1} and B_0 obtained from MLTWA. M is minimised with a grid search in the B_0 and L_e^{-1} parameter space, and the best-fit values $\hat{L}_e^{-1}$ and $\hat{B}_0$ are given by the minima of the function. The isolines of the variable $M_{norm} = M(L_e^{-1}, B_0)/M(\hat{L}_e^{-1}, \hat{B}_0)$ give the error estimates on $\hat{L}_e^{-1}$ and $\hat{B}_0$. Being M_{norm} an F-variable (Del Pezzo and Bianco, 2010), the model parameters can

be estimated using an F distribution (Pisconti et al., 2015), with a level of confidence higher than F=0.68.

4.3.2 Sensitivity kernels

Due to the increased lateral sensitivity compared to ray-dependent techniques, coda waves are theoretically the ideal tool to image the Earth. In practice, apart for the cases of single scattering and diffusion, there is generally no simple analytical solution, and envelopes have to be dealt with Radiative Transfer Theory (Sato et al., 2012), possibly mixed with ray-tracing techniques that model direct wave information (Sanborn et al., 2017). However, if the wavefield is diffusive, one can obtain coda sensitivity kernels with Paasschens equations (Paasschens, 1997) and the approximations of Pacheco and Snieder (2005). Several authors have obtained 2D diffusive kernels based on Radiative Transfer Theory (Obermann et al., 2013; Margerin, 2013; Mayor et al., 2014; Del Pezzo et al., 2016). These kernels have maximum sensitivity at source and receiver (they show a pole at their exact location that must be interpolated) and are all very similar (see e.g. Figs. 4.2) despite being obtained with different approximations. They are primarily aimed at coda-wave interferometry but have found applications in coda-attenuation imaging at regional and local scales (Mayor et al., 2016; De Siena et al., 2017a; Napolitano et al., 2020; Sketsiou et al., 2020). (Calvet et al., 2013) first noticed the contribution of surface waves to low-frequency observations, an effect modelled in 2D by Obermann et al. (2013) and fit on data by Gabrielli et al. (2020). Del Pezzo et al. (2018) have extended the formulation to 3D media, setting the spatial and frequency limits of the kernel applicability and discuss the assumptions behind the applicability of the kernels.

There are two published approaches to map coda attenuation in the 3D space with kernels. The first is regionalization, in analogy to what done in Del Pezzo et al. (2018) and for peak-delay measurements. An excellent review paper on this approach is Del Pezzo and Ibáñez (2020). MuRAT follows instead the pathway laid down by De Siena et al. (2017a). It assumes that all coda energy is contained within the propagation grid at the chose lapse time. If this is true, then coda attenuation in space can be obtained from source-station measurement with a standard inversion. Sketsiou et al. (2020) provides an extensive discussion of the differences between regionalization and inversion. Akande et al. (2019) is the first 3D kernel-based coda attenuation model obtained with 3D sensitivity kernels and an inversion approach.

As anticipated in Chapter 1, the combined effect of coherent and incoherent scattering as well as the trade off induced by changing scattering regimes (from Rayleigh to Mie scattering, Cormier and

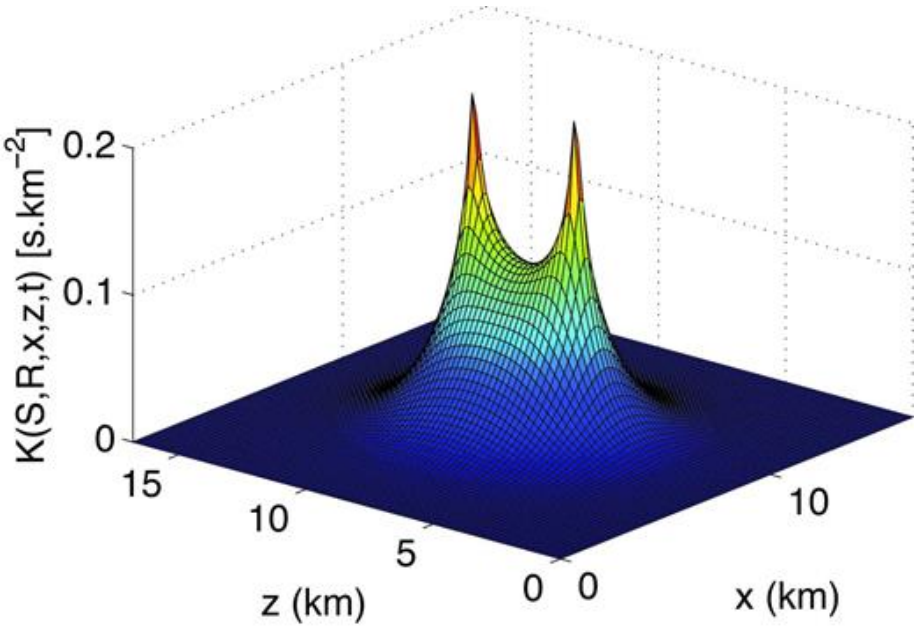

Figure 4.2: Diffusive sensitivity kernels at time 3.6 s obtained by Obermann et al. (2013)

Sanborn (eg 2019)) can deeply affect the reliability of the kernels. In order for these to be applied, there is a need for a volume with uniform (or gradually-changing) scattering properties, which is rarely valid at all frequencies investigated. Surface Obermann et al. (2013) and resonant Margerin (2013); De Siena et al. (2013) waves, sharp horizontal transitions in scattering (Wegler, 2005; Margerin, 2017; Nardoni et al., 2021) and more generally not accounting properly for the trade-offs with geometrical spreading (Morozov, 2011) all bring to inexact, if not incorrect, images of the Earth's scattering and absorption properties.

4.3.3 Applicability

Coda attenuation is measured by MuRAT in the diffusive assumption, hence one must check that Q_c^{-1} does not vary with hypocentral distance (Calvet et al., 2013). However, this only attests that equipartition is in place, a necessary but insufficient condition for diffusion. The analysis of coda attenuation with frequency is central to test the applicability of both MLTWA and sensitivity kernels (Sketsiou et al., 2020). Also, as we are using the inversion procedure, it is central to test that most of coda energy remains inside the inversion grid (Akande et al., 2019).

MuRAT offers tools to test these approximations and the effect of Qc on measurements of total attenuation (chapter 3).

4.3.4 MuRAT workflow

MuRAT works in analogy to Mayor et al. (2016), De Siena et al. (2017a) and Akande et al. (2019) when modelling coda attenuation. These authors show that above 1 Hz one must check the relationship between hypocentral distance and measured coda attenuation. In Figure 4.3, we show the expected relation of coda attenuation versus hypocentral distance for the applicability of the theory and interpretation of Qc as measurement of absorption. It is clear that the standard assumption of twice the S-wave travel time (Aki and Chouet, 1975) does not work. Hence Murat shows you the same plot for your dataset - we will discuss in Chapter ?? the examples at Mount St. Helens and in Vrancea. However, the ideal threshold (100 s in this particular case) removes too many data for reliable coverage. Figures 4.3c shows the acceptable compromise.

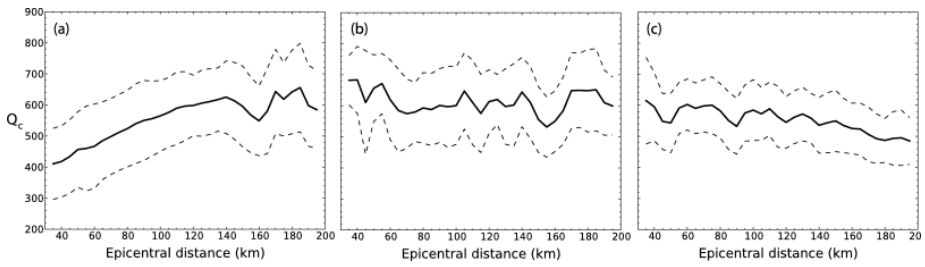

Figure 4.3: (a) Qc as a function of the epicentral distance in the 4–8 Hz frequency band. The duration of the coda window is fixed (t_w = 50 s). The solid and dashed lines show the mean dependence of Qc with the epicentral distance and the associated uncertainties, respectively. The analysis is performed on the onset of coda window t_k equal to (a) 2tS (b) 100 s and (c) 70 s. From Mayor et al. (2016)

MuRAT also outputs the sensitivity kernels in two grids: (1) the fine propagation grid, extending generally well beyond the area of inversion, and (2) the inversion grid. The first is used to compute the full kernels and interpolate the poles at source and receiver locations (Akande et al., 2019). The boundaries of the second are chosen by the user depending on source-station coverage. The code shows what percentage of the energy is still contained inside the inversion grid.

Chapter 5

Getting started

5.1 Matlab

MuRAT wants to be an open-access code, yet it also comes in Matlab format: why?

- The first reason is historical. The code has been designed with core Matlab program, with legacy bash and Fortran codes embedded in it. Passing from Matlab to Python, the obvious choice for open-access interfaces, was not straightforward. Passing from Matlab to Julia has been way easier. Evolving through a decade, the Matlab version of MuRAT has reached the format presented here. Yet, MuRAT3.0 will be the last release in Matlab.
- The second reason is simplicity of learning. MuRAT has been thought from start as a way to introduce students to computational seismology. Matlab an ideal interface to teach computational codes to students in Earth Sciences. MuRAT has also been developed with the wider geological community in mind, which until recently was often lacking training in computation. The average geology student catches Matlab better than other codes.
- The third reason is that Python is becoming the standard in seismology, especially thanks to tools like Obspy, yet this is not so obvious for the rest of Earth Sciences. For example, Matlab is (has been) the favourite language interface for most of the Geodynamics community - see for example Taras Gerya's Introduction to Numerical Geodynamic Modelling. The geodynamics community is embracing Julia as its natural successor. MuRAT does the same.

5.1.1 Requirements and installations

- *DOWNLOAD:* MuRAT from Github. Ideally, fork or star the code to get updates. This guide explains how to work with GitHub Desktop.

- *SYSTEM:* The program works on Mac, Linux and Windows systems equipped with Matlab R2019a or later.
- *NECESSARY TOOLBOXES:* Signal Processing, Curve Fitting, Image Processing and Mapping Toolboxs. The Parallel Computing Toolbox is recommended for speed.
- *EXAMPLE DATASETS:* Three sample datasets (Campi Flegrei, Mount St. Helens and Vrancea) are included in the package and allow the user to obtain sample models. The datasets work with the input **.mlx** files that are provided in the working directory.

5.1.2 The workspace

In this example, MuRAT is cloned from the corresponding page to a folder inside GitHub Desktop. As a developer or user of MuRAT for multiple datasets, you might want to copy this folder on your system at a different location (Fig. 5.1). In the example (Fig. 5.1), we show how you download automatically the main version of the code in a folder contained in the Github folder. Depending on your system, the path to this folder could be different. It is recommended to copy the folder to another path, and leve the original MuRAT folder where it is downloaded. When finished with your work or if cooperating on that specific dataset with someone, you can then substitute your edited folder in Github. This will allow you to push a new branch that might be used as repository for codes and results. These repositories are now a requirement for most journals and allow you to get the seminal version of your results in case of reviews.

5.2 Julia

MuRAT is an open-access code developed from this version onward in Julia: why?

Julia is FAST. Julia is EASY. Julia is more similar to Matlab. Hence, the choice to switch from Matlab to Julia. Is it better than Python? This is an absurd question for two languages developed in different decades. If you need to call a Python script (and sometimes you do), you can do it from Julia. Please have a read at this interesting comparison to know more about how the two codes compare.

a)

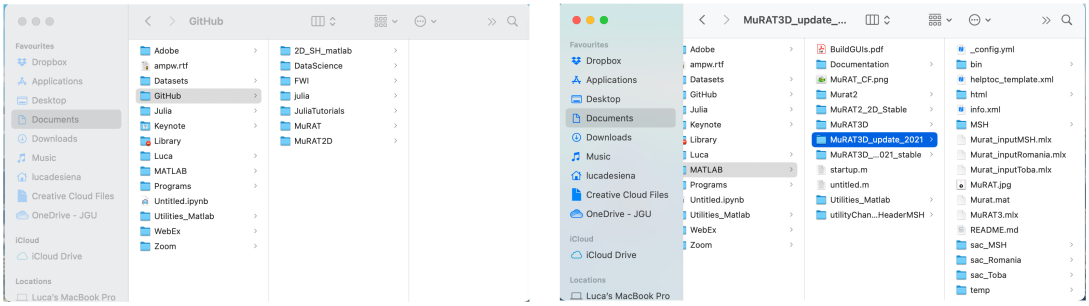

b)

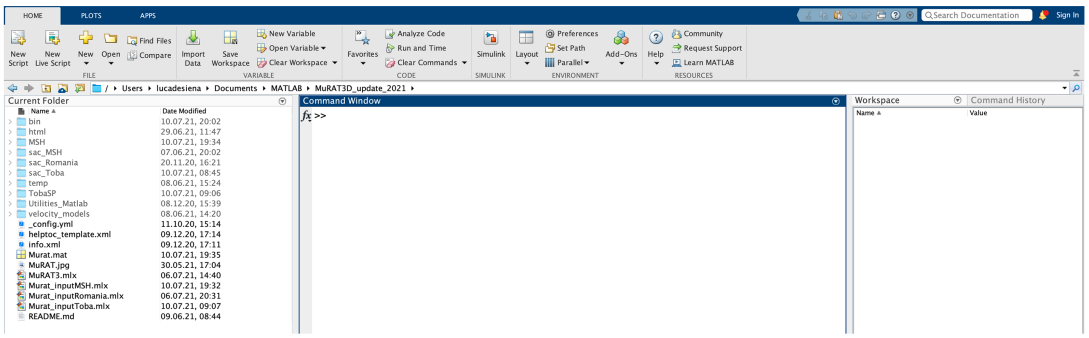

Figure 5.1: How I work with MuRAT in Matlab. a) The folder where the branched code is downloaded (left) vs the working directory (right). b) The Workspace in Matlab. Notice only the Matlab input files are present and must be edited.

5.2.1 Requirements and installations

- *DOWNLOAD:*
- *SYSTEM:*
- *NECESSARY TOOLBOXES:*
- *EXAMPLE DATASETS:*

Bibliography

W. G. Akande, L. De Siena, and Q. Gan. Three-dimensional kernel-based coda attenuation imaging of caldera structures controlling the 1982-84 campi flegrei unrest. *Journal of Volcanology and Geothermal Research*, 381:273–283, 2019.

K. Aki. Attenuation of shear-waves in the lithosphere for frequencies from 0.05 to 25 Hz. *Physics of the Earth and Planetary Interiors*, 21:50–60, 1980.

K. Aki and B. Chouet. Origin of coda waves: Source, attenuation, and scattering effects. *Journal of Geophysical Research*, 80:3322–3342, 1975.

L. V. Block. *Joint hypocenter–velocity inversion of local earthquake arrival time data in two geothermal regions*. Ph.d. dissertation, Massachusetts Institute of Technology, Cambridge, 1991.

M. Calvet and L. Margerin. Lapse time dependence of coda Q: anisotropic multiple-scattering models and application to Pyrenees. *Bulletin of the Seismological Society of America*, 103(3):1993–2010, 2013. doi: $10.1785/0120120239$.

M. Calvet, M. Sylvander, L. Margerin, and A. Villaseñor. Spatial variations of seismic attenuation and heterogeneity in the Pyrenees: Coda Q and peak delay time analysis. *Tectonophysics*, 608:428–439, 2013.

V. F. Cormier and C. J. Sanborn. Trade-offs in parameters describing crustal heterogeneity and intrinsic attenuation from radiative transport modeling of high-frequency regional seismograms. *Bulletin of the Seismological Society of America*, 109(1):312–321, 2019.

L. De Siena, E. Del Pezzo, F. Bianco, and A. Tramelli. Multiple resolution seismic attenuation imaging at Mt. Vesuvius. *Physics of the Earth and Planetary Interiors*, 173:17–32, 2009.

L. De Siena, E. Del Pezzo, and F. Bianco. Campi Flegrei seismic attenuation image: evidences of gas resevoirs, hydrotermal basins and feeding systems. *Journal of Geophysical Research*, 115(B0): 9312–9329, 2010.

L. De Siena, E. Del Pezzo, C. Thomas, A. Curtis, and L. Margerin. Seismic energy envelopes in volcanic media: in need of boundary conditions. *Geophysical Journal International*, 192(1):326–345, 2013.

L. De Siena, C. Thomas, and R. Aster. Multi-scale reasonable attenuation tomography analysis (MuRAT): An imaging algorithm designed for volcanic regions. *Journal of Volcanology and Geothermal Research*, 277:22–35, 2014a.

L. De Siena, C. Thomas, G. P. Waite, S. C. Moran, and S. Klemme. Attenuation and scattering tomography of the deep plumbing system of Mount St. Helens. *Journal of Geophysical Research: Solid Earth*, 119(11):8223–8238, 2014b.

L. De Siena, M. Calvet, K. J. Watson, A. Jonkers, and C. Thomas. Seismic scattering and absorption mapping of debris flows, feeding paths, and tectonic units at Mount St. Helens volcano. *Earth and Planetary Science Letters*, 442:21—31, 2016.

L. De Siena, A. Amoruso, E. D. Pezzo, Z. Wakeford, M. Castellano, and L. Crescentini. Space-weighted seismic attenuation mapping of the aseismic source of Campi Flegrei 1983?1984 unrest. *Geophysical Research Letters*, pages n/a–n/a, 2017a. ISSN 1944-8007. doi: $10.1002/2017\mathrm{GL}072507$. URL `http://dx.doi.org/10.1002/2017GL072507`. 2017GL072507.

L. De Siena, G. Chiodini, G. Vilardo, E. Del Pezzo, M. Castellano, S. Colombelli, N. Tisato, and G. Ventura. Source and dynamics of a volcanic caldera unrest: Campi flegrei, 1983–84. *Scientific reports*, 7(1):1–13, 2017b.

E. Del Pezzo and F. Bianco. Two-layer earth model corrections to the MLTWA estimates of intrinsic- and scattering-attenuation obtained in a uniform half-space. *Geophysical Journal International*, 182 (2):949–955, 2010.

E. Del Pezzo and J. M. Ibáñez. Seismic coda-waves imaging based on sensitivity kernels calculated using an heuristic approach. *Geosciences*, 10(8):304, 2020.

E. Del Pezzo, F. Bianco, L. De Siena, and A. Zollo. Small scale shallow attenuation structure at Mt. Vesuvius. *Physics of the Earth and Planetary Interiors*, 157:257–268, 2006.

E. Del Pezzo, J. Ibañez, J. Prudencio, F. Bianco, and L. De Siena. Absorption and scattering 2-D volcano images from numerically calculated space-weighting functions. *Geophysical Journal International*, 206(2):742–756, 2016.

E. Del Pezzo, A. De La Torre, F. Bianco, J. Ibanez, S. Gabrielli, and L. De Siena. Numerically calculated 3d space-weighting functions to image crustal volcanic structures using diffuse coda waves. *Geosciences*, 8(5):175, 2018.

M. D. P. Di Martino, L. De Siena, D. Healy, and S. Vialle. Petro-mineralogical controls on coda attenuation in volcanic rock samples. *Geophysical Journal International*, 2021.

M. C. Fehler, P. Roberts, and T. Fairbanks. A temporal change in coda wave attenuation observed during an eruption of Mount St. Helens. *Journal of Geophysical Research*, 93:4367–4373, 1988.

M. C. Fehler, M. Hoshiba, H. Sato, and H. Obara. Separation of scattering and intrinsic attenuation for the Kanto-Tokai region, Japan, using mesurements of S-wave energy versus hypocentral distance. *Geophysical Journal International*, 108:787–800, 1992.

M. C. Fehler, H. Sato, and L. J. Huang. Envelope broadening of outgoing waves in 2D random media: a comparison between the Markov approximation and numerical simulations. *Bulletin of the Seismological Society of America*, 90:914–928, 2000.

S. Gabrielli, L. De Siena, F. Napolitano, and E. Del Pezzo. Understanding seismic path biases and magmatic activity at mount st helens volcano before its 2004 eruption. *Geophysical Journal International*, 222(1):169–188, 2020.

P. Ho-Liu, H. Kanamori, and R. W. Clayton. Applications of attenuation tomography to imperial valley and coso-indian wells region, southern california. *Journal of Geophysical Research*, 93(B9): 10501–10520, 1988.

L. Margerin. Diffusion approximation with polarization and resonance effects for the modelling of seismic waves in strongly scattering small-scale media. *Geophysical Journal International*, 192(1): 326–345, 2013.

L. Margerin. Breakdown of equipartition in diffuse fields caused by energy leakage. *The European Physical Journal Special Topics*, 226(7):1353–1370, 2017.

K. Mayeda, S. Koyanagi, M. Hoshiba, K. Aki, and Y. Zeng. A comparative study of scattering, intrinsic and coda q for hawaii, long valley, and central california between 1.5 and 15.0 hz. *Journal of Geophysical Research*, 97:6643–6659, 1992.

J. Mayor, L. Margerin, and M. Calvet. Sensitivity of coda waves to spatial variations of absorption and scattering: radiative transfer theory and 2-d examples. *Geophysical Journal International*, page ggu046, 2014.

J. Mayor, M. Calvet, L. Margerin, O. Vanderhaeghe, and P. Traversa. Crustal structure of the Alps as seen by attenuation tomography. *Earth and Planetary Science Letters*, 439:71–80, 2016.

I. B. Morozov. Geometrical attenuation, frequency dependence of q, and the absorption band problem. *Geophysical Journal International*, 175(1):239–252, 2008.

I. B. Morozov. Mechanisms of geometrical seismic attenuation. *Annals of Geophysics*, 54(3), 2011.

F. Napolitano, L. De Siena, A. Gervasi, I. Guerra, R. Scarpa, and M. La Rocca. Scattering and absorption imaging of a highly fractured fluid-filled seismogenetic volume in a region of slow deformation. *Geoscience Frontiers*, 11(3):989–998, 2020.

C. Nardoni, L. De Siena, F. Cammarano, F. Magrini, and E. Mattei. Modelling regional-scale attenuation across italy and the tyrrhenian sea. *Physics of the Earth and Planetary Interiors*, page 106764, 2021.

K. Nishigami. A new invertion method of coda waveforms to determine spatial distribution of coda scatterers in the crust and uppermost mantle. *Geophysical Research Letters*, 12(18):2225–2228, 1991.

A. Obermann, T. Planes, E. Larose, C. Sens-Schönfelder, and M. Campillo. Depth sensitivity of seismic coda waves to velocity perturbations in an elastic heterogeneous medium. *Geophysical Journal International*, 194(1):372–382, 2013.

J. C. L. Paasschens. Solution of the time-dependent Boltzmann equation. *Physical Review*, 56(1): 1135–1141, 1997.

C. Pacheco and R. Snieder. Time-lapse travel time change of multiply scattered acoustic waves. *The Journal of the Acoustical Society of America*, 118(3):1300–1310, 2005.

A. Pisconti, E. Del Pezzo, F. Bianco, and S. de Lorenzo. Seismic q estimates in umbria marche (central italy): hints for the retrieval of a new attenuation law for seismic risk. *Geophysical Journal International*, 201(3):1370–1382, 2015.

J. Prudencio, J. M. Ibáñez, A. García-Yeguas, E. Del Pezzo, and A. M. Posadas. Spatial distribution of intrinsic and scattering seismic attenuation in active volcanic islands–ii: Deception island images. *Geophysical Journal International*, 195(3):1957–1969, 2013.

J. Prudencio, L. De Siena, J. Ibáñez, E. Del Pezzo, A. García-Yeguas, and A. Díaz-Moreno. The 3D Attenuation Structure of Deception Island (Antarctica). *Surveys in Geophysics*, 36(3):371–390, 2015.

T. Saito, H. Sato, and M. Ohtake. Envelope broadening of spherically outgoing waves in three-dimensional random media having power law spectra. *Journal of Geophysical Research*, 107(B5): 2089–2103, 2002.

C. J. Sanborn, V. F. Cormier, and M. Fitzpatrick. Combined effects of deterministic and statistical structure on high-frequency regional seismograms. *Geophysical Journal International*, 210(2):1143–1159, 2017.

H. Sato. Broadening of seismogram envelopes in the randomly inhomogeneous lithosphere based on the parabolic approximation: southeastern Honshu, Japan. *Journal of Geophysical Research*, 94: 17735–17747, 1989.

H. Sato. Envelope broadening and scattering attenuation of a scalar wavelet in random media having power-law spectra. *Geophysical Journal International*, 204(1):386–398, 2016.

H. Sato, M. C. Fehler, and T. Maeda. *Seismic Wave Propagation and Scattering in the heterogeneous Earth: Second Edition*. Springer, New York, USA, 2012.

P. Sketsiou, F. Napolitano, A. Zenonos, and L. De Siena. New insights into seismic absorption imaging. *Physics of the Earth and Planetary Interiors*, 298:106337, 2020.

P. Sketsiou, L. De Siena, S. Gabrielli, and F. Napolitano. 3-d attenuation image of fluid storage and tectonic interactions across the pollino fault network. *Geophysical Journal International*, 226(1): 536–547, 2021.

T. Takahashi, H. Sato, T. Nishimura, and K. Obara. Strong inhomogeneity beneath Quaternary volcanoes revealed from the peak delay analysis of S-wave seismograms of microearthquakes in northeastern Japan. *Geophysical Journal International*, 168(1):90–99, 2007.

T. Takahashi, H. Sato, T. Nishimura, and K. Obara. Tomographic inversion of the peak delay times to reveal random velocity fluctuations in the lithosphere: method and application to northeastern japan. *Geophysical Journal International*, 178(3):1437–1455, 2009.

S. Takemura, T. Furumura, and T. Saito. Distortion of the apparent s-wave radiation pattern in the high-frequency wavefield: Tottori-ken seibu, japan, earthquake of 2000. *Geophysical Journal International*, 178(2):950–961, 2009.

J. N. Tripathi, M. Sato, and M. Yamamoto. Envelope broadening characteristics of crustal earthquakes in northeastern Honshu, Japan. *Geophysical Journal International*, 182(2):988–1000, 2010.

U. Wegler. Diffusion of seismic waves in layered media: boundary conditions and analytic solutions. *Geophysical Journal International*, 163:1123–1135, 2005.

U. Wegler and B. G. Lühr. Scattering behaviour at Merapi Volcano (Java) revealed from an active seismic experiment. *Geophysical Journal International*, 145:579–592, 2001.

J. Xie. Can we improve estimates of seismological q using a new "geometrical spreading" model? *Pure and Applied Geophysics*, 167(10):1147–1162, 2010.

K. Yoshimoto, H. Sato, and M. Ohtake. Frequency-Dependent Attenuation of P and S Waves in the Kanto Area, Japan, based on the Coda-Normalization Method. *Geophysical Journal International*, 114:165–174, 1993.